UNIVERSITY *of York*

This is a repository copy of *Laser Wakefield Accelerator modelling with Variational Neural Networks*.

White Rose Research Online URL for this paper:
https://eprints.whiterose.ac.uk/225390/

Version: Published Version

Article:

Streeter, M. J.V., Colgan, C., Cobo, C. C. et al. (23 more authors) (2023) Laser Wakefield Accelerator modelling with Variational Neural Networks. High Power Laser Science and Engineering. e9. ISSN 2052-3289

https://doi.org/10.1017/hpl.2022.47

White Rose
university consortium
Universities of Leeds, Sheffield & York

eprints@whiterose.ac.uk
https://eprints.whiterose.ac.uk/

HIGH POWER LASER
SCIENCE AND ENGINEERING

RESEARCH ARTICLE

Laser wakefield accelerator modelling with variational neural networks

M. J. V. Streeter [1], C. Colgan[2], C. C. Cobo [3], C. Arran[3], E. E. Los[2], R. Watt [2], N. Bourgeois[4],

L. Calvin[1], J. Carderelli[5], N. Cavanagh[1], S. J. D. Dann[4], R. Fitzgarrald[5], E. Gerstmayr [2],

A. S. Joglekar [5,6], B. Kettle [2], P. Mckenna [7], C. D. Murphy[3], Z. Najmudin[2], P. Parsons[4], Q. Qian[5],

P. P. Rajeev[4], C. P. Ridgers[3], D. R. Symes[4], A. G. R. Thomas[5], G. Sarri[1], and S. P. D. Mangles[2]

[1] *School of Mathematics and Physics, Queen's University Belfast, Belfast, UK*

[2] *The John Adams Institute for Accelerator Science, Imperial College London, London, UK*

[3] *York Plasma Institute, School of Physics, Engineering and Technology, University of York, York, UK*

[4] *Central Laser Facility, STFC Rutherford Appleton Laboratory, Didcot, UK*

[5] *Gérard Mourou Center for Ultrafast Optical Science, University of Michigan, Ann Arbor, USA*

[6] *Ergodic LLC, San Francisco, USA*

[7] *Department of Physics, SUPA, University of Strathclyde, Glasgow, UK*

Abstract
A machine learning model was created to predict the electron spectrum generated by a GeV-class laser wakefield accelerator. The model was constructed from variational convolutional neural networks, which mapped the results of secondary laser and plasma diagnostics to the generated electron spectrum. An ensemble of trained networks was used to predict the electron spectrum and to provide an estimation of the uncertainty of that prediction. It is anticipated that this approach will be useful for inferring the electron spectrum prior to undergoing any process that can alter or destroy the beam. In addition, the model provides insight into the scaling of electron beam properties due to stochastic fluctuations in the laser energy and plasma electron density.

Keywords: laser plasma interactions; particle acceleration; neural networks; machine learning

1. Introduction

Laser wakefield accelerators (LWFAs) generate multi-GeV electron beams from cm-scale plasma channels using approximately 100 TW laser pulses[1–6]. The extreme acceleration gradients of LWFAs, coupled with their relative accessibility, have led to widespread research and pursuit of several applications, such as compact light sources[7–10], generation of bright γ-rays[11] and ultra-relativistic positron beams[12], and for future particle colliders[13]. Also, the combination of GeV electron beams and high-intensity laser pulses allows for the study of fundamental physics such as strong-field quantum electrodynamics[14–17].
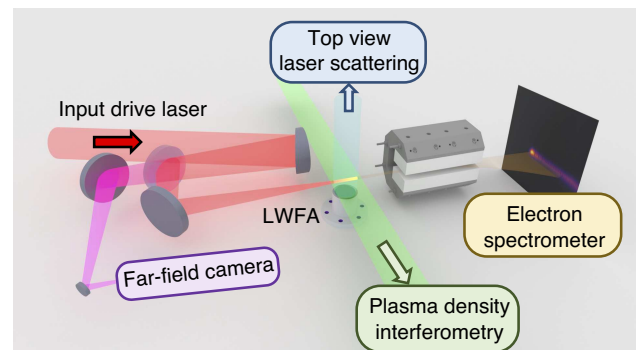
In LWFAs, the non-linear laser pulse evolution[18,19] and its effect on the injection and acceleration processes[20–23] are highly sensitive to the initial conditions and can lead to significant shot-to-shot variation of the electron beam properties[24,25]. Recent work on high-stability laser systems and plasma sources has demonstrated improved stability, with the observation of few-percent variation in the electron beam energy and charge over 24 hours of continuous operation[26]. Long-term high-repetition rate operation has opened up the possibility of using machine learning techniques to model the sources of electron beam variation and to use closed-loop algorithms to optimise performance[26–31].

For applications such as the study of the radiation reaction, knowledge of the pre-interaction electron beam properties is required to make precise measurements of any changes of these properties and thereby infer the validity of theoretical

Correspondence to: M. J. V. Streeter, School of Mathematics and Physics, Queen's University Belfast, BT7 1NN Belfast, UK. Email: m.streeter@qub.ac.uk

1

models[32–34]. The destructive nature of the measurements necessitates predictable LWFA performance through one of the following: improved stability; preserving part of the spectrum as a reference[33]; or by developing models capable of producing the electron beam properties from a given shot. In general, the ability to make predictions of the outputs from plasma accelerators will be advantageous to many of their applications.

Previous work in developing machine learning models for LWFAs has demonstrated the prediction of scalar metrics of the electron beam, such as total charge or peak energy[29–31,35]. However, many applications will require the prediction of vector properties, such as the spectrum or the longitudinal phase space, for which neural networks provide a convenient framework. A densely connected neural network (DNN) is made of densely connected layers, in which every input is the weighted sum of all of the outputs of the previous layer, with the individual weights as free parameters of the model. A non-linear activation function (e.g., a sigmoid function) then takes the weighted sum plus a bias value (another free model parameter) as its argument and returns an output value. An alternative to deeply connected layers is a convolutional layer, which performs convolutions between the input vector and a set of kernels. Networks using these layers, known as convolutional neural networks (CNNs), have been shown to be better suitable for learning meaningful features from natural signals[36]. Further improvement to the predictive power of neural networks has been seen when including stochasticity in the outputs of individual nodes, in an architecture known as a variational neural network (VNN)[37].

In conventional accelerators, Emma *et al.*[38] demonstrated training of a DNN to produce synthetic diagnostic outputs that matched the measured outputs for a new unseen dataset. CNNs have been used to predict X-ray properties from the post-undulator electron beam spectrum[39], while ensembles of DNNs have also been used to predict the electron beam longitudinal phase space and current profile from non-destructive bending radiation measurements[40]. In this work, we report on the training of an ensemble of VNNs to model the LWFA-generated electron spectrum using secondary diagnostics of the laser and plasma conditions. The LWFA ensemble was trained using a subset of experimental measurements of the electron spectrum with the remainder used for model validation. Each individual VNN in the ensemble was trained with a different subset of the training data, so that the ensemble provided both a mean prediction and an estimate of its uncertainty. The model also reveals the extent to which the measurements obtained from the available diagnostics are predictive of the accelerator performance, and which parameters have the strongest influence.

2. Experimental methods and results

The experiment was performed using the Gemini laser system at the Central Laser Facility in the UK (see Figure 1 for details). Laser pulses with an energy of $E_L = (6.6 \pm 0.5)$ J and a pulse duration of approximately equal to 50 fs were used to drive a GeV-scale LWFA. The pulses were focused with an $f/40$ off-axis parabolic mirror to a spot size of $(50 \pm 2) \times (45 \pm 2)$ μm in the horizontal (polarisation) and vertical planes, respectively, giving a peak intensity of $(5.5 \pm 0.5) \times 10^{18}$ W cm^{-2}. The focus was aligned to a gas jet that was composed of a mixture of 2% nitrogen and 98% helium, enabling ionisation injection[41–44]. The gas jet had an average electron density of $(1.00 \pm 0.07) \times 10^{18}$ cm^{-3} over a 17 mm length.

The LWFA-generated electron energy spectrum dW/dE was measured using the spectrometer scintillator screen images, which were energy-calibrated by numerical tracking of electron trajectories in the magnetic field. The interferometry and top view cameras were used to extract the electron density profile, $n_e(z)$, and the laser scattering profile, $S_L(z)$, respectively, where z is the laser propagation axis. A 2D Gaussian fit was performed on the far-field image to obtain six parameters: the peak fluence I_0; the centroids x_0 and y_0; the major and minor root-mean-square (RMS) spot widths σ_a and σ_b; and the angle of the major axis of the ellipse with x-axis θ. Due to the aberrations and clips caused by this beam-line, this far-field is not an exact replica of the main

Figure 1. Illustration of the experimental setup (not to scale). The primary laser focus was aligned to the front edge of a supersonic gas jet emitted from a 15 mm diameter nozzle positioned 10 mm below the laser pulse propagation axis. The input laser energy was measured by integrating the signal on a near-field camera before the compressor, which was cross-calibrated with an energy meter and adjusted for the 60% compressor throughput. The scattered laser signal was observed from above by an optical camera, and the plasma channel electron density profile was measured using interferometry with a transverse short-pulse probe laser. The small ($\lesssim 0.1\%$) transmission of the focusing laser pulse through a dielectric mirror was directed onto a CCD camera to obtain an on-shot far-field image. Electron beams from the LWFA were deflected by a magnetic dipole onto two Lanex screens (only the first is shown here), which were used to determine the electron spectrum in the range of $0.3 < E < 2.5$ GeV.

laser focus, but is representative of the shot-to-shot focal spot fluctuations.

The experimental results for this analysis were taken from an investigation of the radiation reaction, in which a second counter-propagating laser pulse is used to collide with the LWFA electron beam. For training and validating our predictive tool, we wish to only use shots where the laser pulse did not significantly overlap with the electron beam, so that the electron spectrum was not affected. For successful collisions, a gamma-beam was generated via the inverse Compton scattering interaction and was diagnosed spatially with a CsI scintillator array[16] imaged onto a 1024×1024 pixels charge-coupled device (CCD).

Due to the shot-to-shot variation in the electron beam position, most shots did not result in a significant collision, providing a large number of null shots for model training and testing. The brightness of the signal on the gamma detector was used to provide an approximate metric of the collision intensity. The 99.99th percentile pixel value of the background subtracted CCD image was taken as the peak of the gamma signal C_γ. The highest value of this metric was $C_\gamma = 4380$, whereas the median value was $C_\gamma = 12$. From analysis of the collision statistics, a value of $C_\gamma \leq 100$ was estimated to result from collisions with a peak normalised vector potential of $a_0 < 1.4$. For 1 GeV electrons, this would result in a less than 1% energy loss[14], approximately equal to the resolution of the spectrometer. Therefore, this value was taken as a threshold for null shots, for which the electron beam is unaffected by the collision. The experimental data were taken during a 5-hour period with a total of 779 shots. Model training and validation datasets were taken from shots for which $C_\gamma \leq 100$, with 90% (570 shots) used for training and 10% (75 shots) reserved for model validation.

3. Neural network architecture and training

The measurements of $n_e(z)$, $S_L(z)$ and dW/dE were stored as 1D vectors of lengths 310, 100 and 200, respectively.

Although each of these signals is composed of at least 100 values, the variations over the full dataset are limited, and so in principle only a few parameters are required for each to encode these variations. An appropriate decoder would be able to generate a good approximation to the measured signals from this reduced set of parameters, which are called latent space variables. In this work, variational autoencoders (VAEs)[45,46] incorporating convolutional and densely connected layers were trained, as illustrated in Figure 2. By using a bottleneck of only a few nodes, the VAEs were trained to find an optimal latent space representation of the data, which allowed the decoder to reconstruct the measured signals.

The trained encoders for $n_e(z)$ and $S_L(z)$ were used to encode their respective measurements to their latent space representations, which were then combined with measurements of the laser far-field and the laser energy to create the inputs for the predictive model. A VNN, which we call the translator network, takes those inputs and returns values that are passed to the trained electron spectra decoder to generate the predicted spectrum. The translator was trained to learn the correlation between the reduced input set and the latent variables of the electron spectra decoder, as illustrated in Figure 3.

For the variational layers, two parameters are calculated for each node that represent the expectation value μ_m and standard deviation σ_m. During training, values were sampled from Gaussian distributions given by these parameters, $\mathcal{N}(\mu_m, \sigma_m)$, such that the latent values for a given input set, x_m, would vary according to σ_m.

The training loss function used was as follows[45]:

$$\mathcal{L}_T = \mathcal{L}_{MSE} - \beta D_{KL},$$

$$\mathcal{L}_T = \frac{1}{N} \sum_{n=0}^{N} [W(E_n) - W_R(E_n)]^2 - \beta D_{KL}, \qquad (1)$$

where $D_{KL} = \sum_{m=0}^{M} [1 + \log(\sigma_m) - \mu_m^2 - \sigma_m]/(2M)$ is the Kullback–Leibler (KL) divergence, $\mathcal{L}_{MSE}$ is the mean
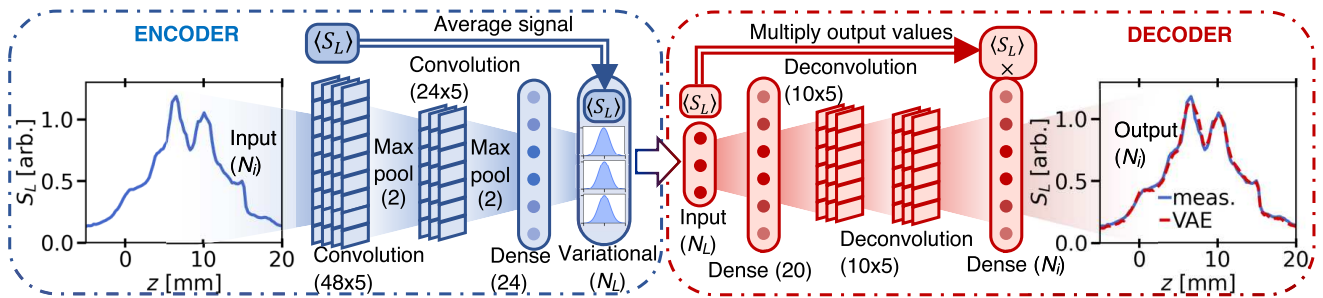

Figure 2. Variational autoencoder (VAE) architecture for determining the latent space representation of the diagnostics. The type and dimension of each layer are indicated in the labels. The inset plots show an example laser scattering signal S_L and the approximation returned by the VAE. The input (and output) size N_i is equal to the data binning of the results for each individual diagnostic. Max pooling was used at the output of each convolution layer, which combined neighbouring output pairs and returned only the maximum of each pair. The average signal, in this case $\langle S_L \rangle$, was passed as an additional latent space parameter for the encoder and was used to scale the output of the decoder. The autoencoder structure was the same for each diagnostic, except for the size of the latent space.
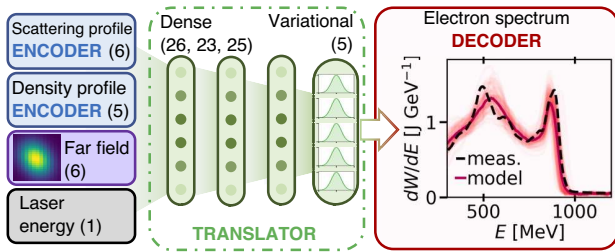
Figure 3. Diagram of the translator network architecture. Shown in the inset is an example measurement from the experimental data (black), with the mean prediction of the LWFA model ensemble (red) and individual model predictions (pink).

squared error (MSE) and M is the total number of input sets in a given training iteration. The same loss function was used to train each VAE and also the final translator VNN, with the MSE taken between the predicted and measured diagnostic output ($n_e(z)$, $S_L(z)$ or dW/dE). The β parameter was used to scale the relative importance of the regularisation, following the beta-VAE approach[45]. During model validation, only the mean weights for the variational layers were used and the D_{KL} term from Equation (1) was omitted. Every node of the neural networks used the leaky rectified linear unit (leaky-ReLU)[47] activation function with $\alpha = 0.3$, which exhibited superior learning performance in comparison to sigmoid and hyperbolic tan functions, as well as leaky-ReLU with other values of α.

For the diagnostic VAEs, the number of latent parameters was chosen to be the minimum that gave high-fidelity reconstructions, with the β parameter manually tuned to ensure that the distribution of each latent parameter for the training datasets was close to a standard normal distribution ($\mathcal{N}(0, 1)$). One latent space parameter was directly set as the average of the input signal (normalised by the training dataset). This parameter was then used to scale the decoder output and ensured that one of the latent space variables represents the amplitude of the signal, aiding interpretation of the trained networks. Once the VAEs were trained, the weights were frozen during the translator training process.

The translator is a DNN with a variational last layer. The translator VNN architecture (number of nodes and number of layers) and the value of β were optimised using a genetic

algorithm. During this process the training data were divided in two parts, with 50% of the data used to train each network and the other 50% used to calculate the test loss. This ensured that the validation dataset was kept purely for validation of the final model performance and not used in any tuning of the predictive model. The optimal architecture for the translator network, shown in Figure 3, comprises three densely connected layers, with a final variational layer with five outputs.

In order to quantify the uncertainty in the model predictions, 100 translator VNNs were trained, each using randomly selected 50% samples of the training dataset. The prediction of each of these models can then be used to obtain an average prediction, while the variation between model predictions is indicative of the random uncertainty and the finite size of the training data. In particular, the random sub-sampling affects the predictive quality in regions where the training data are sparse, typically at the extremes of the input parameters, resulting in a larger uncertainty in those regions.

The parameters for the trained VAEs and translator networks are summarised in Table 1. Each autoencoder was trained for 1000 iterations with a batch size of 64. The translator network was trained in three stages with 200, 400 and 300 iterations performed at 10, 4 and 1 times the final β value to balance reconstruction fidelity with latent space smoothness[46]. The training processes were all performed using the Adam optimiser[48], with a learning rate of 10^{-3}, which was found to converge well.

4. LWFA prediction results

The measured electron spectra from the validation dataset are shown in Figure 4(a), along with the reconstructions by the electron spectra VAE (Figure 4(b)) and the average of the LWFA model ensemble predictions (Figure 4(c)). The electron spectra VAE had an MSE of 0.011, and shows good qualitative and quantitative reproduction of the measured electron spectra. This indicates that the five parameters of the latent space, in combination with the structures learnt by the decoder, are sufficient to accurately generate the set of observations from the validation dataset. In other words, the five latent parameters are sufficient to generate the full

Table 1. Summary of autoencoder parameters used for each diagnostic and for the translator model.

Model	N_i	N_L	β	Validation $\mathcal{L}_{MSE}$
Density profile	310	4+1	2×10^{-3}	1.7×10^{-3}
Scattering profile	100	5+1	10^{-3}	2.3×10^{-3}
Electron spectra	200	4+1	2×10^{-3}	1.1×10^{-2}
LWFA single	18	5	$^a 5 \times 10^{-4}$	$(7.3 \pm 0.5) \times 10^{-2}$
LWFA ensemble	18	5	$^a 5 \times 10^{-4}$	5.7×10^{-2}

^{a}For the LWFA translator models, the value of β varied from high to low during the training, with the final value given in the table. The training time for each autoencoder was 10 minutes and training of the 100 translator networks took a total of 3 hours, using an Intel Xeon Gold 6130 CPU at 2.1 GHz with 32 GB of RAM. The analysis and model training were performed on CLF Data Analysis as a Service (CDAS)[49]. The neural networks were built using the Keras API (https://keras.io).
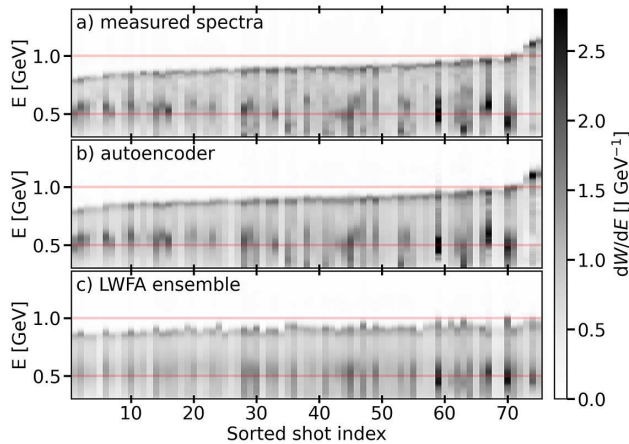
Figure 4. (a) Measured electron spectra and reproduced electron spectra using (b) the trained variational autoencoder and (c) the mean prediction of the ensemble of the LWFA models. The individual shots are sorted by cut-off energy, determined as the highest energy for which the spectra exceed a threshold value.

variability of electron beams for this experimental setup. The question is then whether the secondary diagnostics are sufficient to determine the correct latent variables for each shot and thereby give an accurate prediction of the electron spectrum. The mean prediction of the LWFA model ensemble had an MSE of 0.057 and shows a similar trend in cut-off energy to the data, except for the few high- and low-energy outliers. By comparison, a naive prediction that all measured spectra are equal to the average spectrum from the training dataset gives an MSE value of 0.11, indicating that the LWFA model has a significant predictive capability.

Individual predictions of each model of the LWFA ensemble, along with the corresponding measured electron spectra, are shown in Figure 5. The variation in model predictions for a given shot is indicative of the uncertainty, due to the random sub-sampling of the training data and the stochastic training process. For a large region of the parameter space, the LWFA model predictions show a good agreement with the measurements, with large discrepancies occurring for the outliers in terms of cut-off energy. These shots also exhibit the largest variation in predictions between individual models within the ensemble. The total electron beam energy is reasonably accurately predicted, with relative RMS error of 12% for the entire validation dataset, compared to the relative beam energy RMS variation of 30%.

The relative influence of each input parameter on the LWFA model can be seen by varying each one in turn and measuring the effect on the resultant spectrum, as shown in Figure 6. The plasma density parameters have a relatively modest effect on the electron spectrum, indicating that the shot-to-shot variation of the plasma density profile is not the dominant contributor to the electron spectrum variation. Variations of the laser energy and the scattering profile are more significant, having the greatest effect on the generated
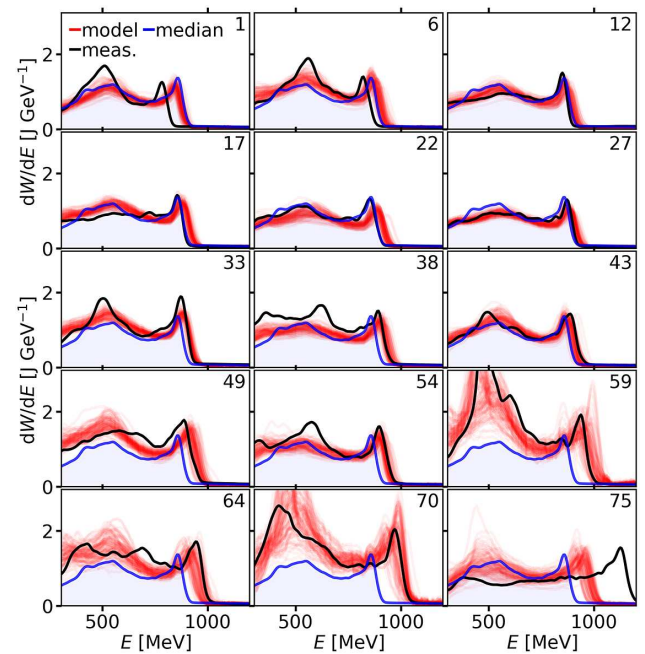

Figure 5. Individual shots selected at equally spaced intervals of the sorted shot index from Figure 4. The measured spectra (black) are shown alongside the predictions of each LWFA model from the trained ensemble (red) and an individual spectrum measurement closest to the median of the training data (blue). The sorted shot index is shown in the top right of each panel.
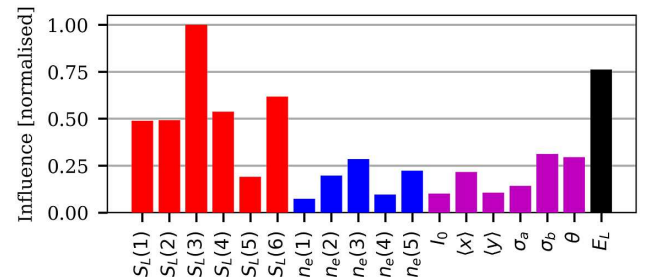

Figure 6. Relative influence of the translator VNN input parameters on the predicted electron spectra. Each parameter is set to the mean value of the training dataset and then varied over ± 3 standard deviations in 11 steps, with the variation in the spectrum quantified by the average RMS change to the spectrum. The nth latent space parameters for the scattering and density profile encoders are labelled $S_L(n)$ and $n_e(n)$, respectively. Here, $S_L(6)$ and $n_e(5)$ are proportional to the average laser scattering signal and plasma electron density, respectively.

electron spectra. The spatio-temporal distribution of the laser pulse is only indirectly diagnosed from the far-field diagnostic and the effect on the scattering profile, and is known to have a large influence on the accelerated electrons[26,28,29]. Including additional laser diagnostics, such as measurement of the spatial phase profile[26,30], should enable higher fidelity predictions.

Although many of the input parameters are not straightforward to interpret physically, that is, those that are the latent space of the autoencoders, the laser energy is a physically important parameter in LWFAs. In practice, the inputs for the LWFA models are not independent of one
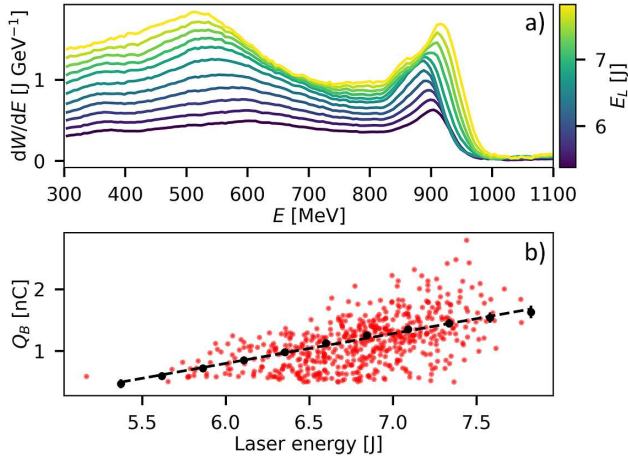
Figure 7. The model predicted effect of varying the laser energy on (a) the predicted electron spectra and (b) the total electron beam charge. The data for each shot in the training data (red) are shown in (b), overlaid from the values calculated from the predicted spectra of the LWFA model (black points) with a linear fit (black dashed line).

Figure 8. The effect of changing $n_e(5)$ on (a) the electron density profile and (b) the predicted electron spectrum. All other latent space parameters are kept fixed at zero (i.e., their average values from the training dataset), while $n_e(5)$ is varied over the range of ± 3 standard deviations in the training dataset.

Figure 9. The effect of changing $S_L(3)$ on (a) the laser scattering profile and (b) the predicted electron spectrum. All other latent space parameters are kept fixed at zero (i.e., their average values from the training dataset), while $S_L(3)$ is varied over the range of ± 3 standard deviations in the training dataset.

another, as characterised by calculating the Pearson correlation coefficients for the training dataset. This reveals relatively strong correlations between the laser energy and several other parameters, especially $S_L(3)$, $S_L(4)$, $S_L(6)$, $n_e(4)$, $n_e(5)$ and I_0, which had correlation coefficients ranging from $r = 0.31$ to $r = 0.55$. The trained LWFA model is then able to show what effect laser energy fluctuations have on the electron spectrum by varying each parameter proportionally according to their correlation coefficients with laser energy E_L, as shown in Figure 7(a). As the laser energy increases, the peak electron energy is relatively constant, while the overall charge increases. The total electron beam charge Q_B is plotted as a function of laser energy in Figure 7(b), for both the raw data and the LWFA model predictions. The model prediction shows an approximately linear increase with laser energy with the equation $Q_B \, [\text{nC}] = 0.48 E_L \, [\text{J}] - 2.1$.

The scaling parameters $S_L(6)$ and $n_e(5)$ are also easy to interpret, as they are the average scattering signal and electron density, respectively (normalised to the mean and variance over the training dataset). The effect of $n_e(5)$ on the electron density profile and the predicted electron spectrum is shown in Figure 8. The average plasma electron density varied by 4% over the training dataset, as illustrated by the small perturbations to the density profile observed in Figure 8(a). A more significant effect is seen on the electron spectra in Figure 8(b), with the peak energy shifting higher as the average density drops, as expected for a dephasing-limited LWFA[50,51]. The effect on the spectrum is much smaller than that seen to be caused by the laser energy variation in Figure 7. This indicates that the level of natural variations of the plasma electron density in this dataset was sufficiently low that it was not a dominant contributor to the shot-to-shot variations in the electron spectra.
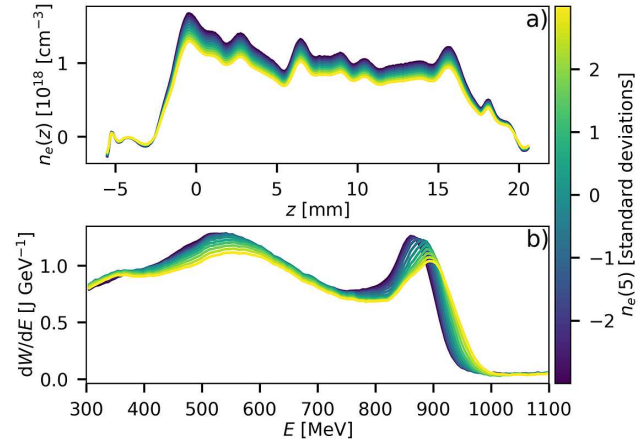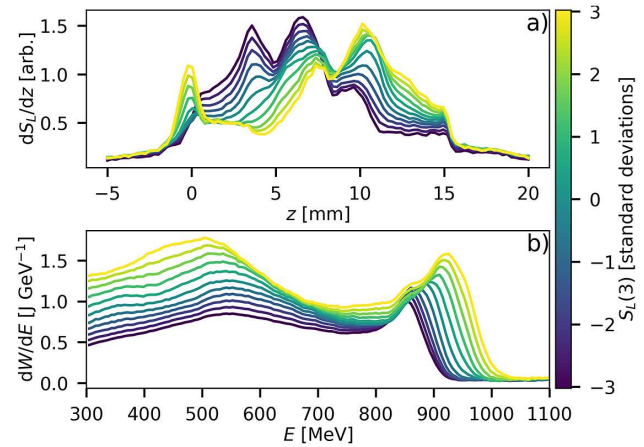
The other latent parameters generated by the VAEs do not have straightforward physical interpretations and only have meaning in combination with the trained encoders. In order to gain some insight into their physical meaning, the effect of changing each parameter can be observed on the corresponding diagnostic output, as well as on the predicted electron spectrum. An example is shown in Figure 9, where the effect of varying $S_L(3)$, the most dominant input parameter to the translator VNN, is shown.

Figure 9(a) shows that positive $S_L(3)$ correlates with an increased laser scattering peak at the entrance to the gas jet ($z = 0$) and for the last half of the plasma, while suppressing the signal for $1 > z > 7$ mm. This also results in an increased predicted total charge as well as an increased predicted maximum electron energy (see Figure 9(b)), a clearly beneficial effect for many applications. The scattered

laser intensity is associated with Raman side-scattering and wavebreaking radiation, generated as the laser self-guides and self-compresses to a high peak intensity in the plasma channel[52,53]. Therefore, the increase of this scattering signal seen in Figure 9(a) indicates an increased possibility for the injection of electrons into the plasma wakefield at $z = 0$ mm, while maintaining a high amplitude plasma wave for $z > 7$ mm, resulting in the enhanced electron spectrum predicted in Figure 9(b).

5. Conclusion

In conclusion, we have constructed and trained a predictive model for an LWFA that is capable of predicting the electron spectrum for a given shot, based on secondary diagnostics of the laser and plasma conditions. The model is constructed from separately trained variational convolutional autoencoders, with a VNN used to map a reduced parameter set to the latent space of an electron spectra decoder. An ensemble of models was trained on subsets of the training data, with the range of model predictions providing an estimate of the uncertainty. The predictive model ensemble performs better than the naive assumption that the electron spectrum is constant, and so has utility in estimating the electron spectrum in the case of destructive processes, such as a radiation reaction. The model fidelity is most likely limited by the lack of on-shot spatio-temporal information about the laser pulse, which is known to have a strong influence on the accelerated electron beam[26]. It is expected that this technique can be improved by including additional diagnostics of the laser spatial and spectral phase, and by increasing the size of the training dataset, especially for reducing the prediction error for the outliers. Further diagnostics of the laser–plasma interaction, such as spectrally resolving the scattering signal, may also provide additional information to improve the prediction accuracy. Neural networks of this kind could be an important tool for understanding the performance sensitivities of plasma accelerators, and also in providing synthetic diagnostics for applications of their electron beams and secondary sources.

Data availability

The data and code for this publication are available from the online repository zenodo.org at https://zenodo.org/record/7510352#.Y9K2XezP30o.

References

1. W. P. Leemans, B. Nagler, A. J. Gonsalves, C. Tóth, K. Nakamura, C. G. R. Geddes, E. Esarey, C. B. Schroeder, and S. M. Hooker, Nat. Phys. **2**, 696 (2006).
2. S. Kneip, S. R. Nagel, S. F. Martins, S. P. D. Mangles, C. Bellei, O. Chekhlov, R. J. Clarke, N. Delerue, E. J. Divall, G. Doucas, K. Ertel, F. Fiuza, R. Fonseca, P. Foster, S. J. Hawkes, C. J. Hooker, K. Krushelnick, W. B. Mori, C. A. J. Palmer, K. T. Phuoc, P. P. Rajeev, J. Schreiber, M. J. V. Streeter, D. Urner, J. Vieira, L. O. Silva, and Z. Najmudin, Phys. Rev. Lett. **103**, 035002 (2009).
3. C. E. Clayton, J. E. Ralph, F. Albert, R. A. Fonseca, S. H. Glenzer, C. Joshi, W. Lu, K. A. Marsh, S. F. Martins, W. B. Mori, A. Pak, F. S. Tsung, B. B. Pollock, J. S. Ross, L. O. Silva, and D. H. Froula, Phys. Rev. Lett. **105**, 105003 (2010).
4. X. Wang, R. Zgadzaj, N. Fazel, Z. Li, S. A. Yi, X. Zhang, W. Henderson, Y.-Y. Chang, R. Korzekwa, H.-E. Tsai, C.-H. Pai, H. Quevedo, G. Dyer, E. Gaul, M. Martinez, A. C. Bernstein, T. Borger, M. Spinks, M. Donovan, V. Khudik, G. Shvets, T. Ditmire, and M. C. Downer, Nat. Commun. **4**, 1988 (2013).
5. W. P. Leemans, A. J. Gonsalves, H.-S. Mao, K. Nakamura, C. Benedetti, C. B. Schroeder, C. Tóth, J. Daniels, D. E. Mittelberger, S. S. Bulanov, J.-L. Vay, C. G. R. Geddes, and E. Esarey, Phys. Rev. Lett. **113**, 245002 (2014).
6. A. J. Gonsalves, K. Nakamura, J. Daniels, C. Benedetti, C. Pieronek, T. C. H. de Raadt, S. Steinke, J. H. Bin, S. S. Bulanov, J. van Tilborg, C. G. R. Geddes, C. B. Schroeder, C. T/oth, E. Esarey, K. Swanson, L. Fan-Chiang, G. Bagdasarov, N. Bobrova, V. Gasilov, G. Korn, P. Sasorov, and W. P. Leemans, Phys. Rev. Lett. **122**, 084801 (2019).
7. H. P. Schlenvoigt, K. Haupt, A. Debus, F. Budde, O. Jäckel, S. Pfotenhauer, H. Schwoerer, E. Rohwer, J. G. Gallacher, E. Brunetti, R. P. Shanks, S. M. Wiggins, and D. A. Jaroszynski, Nat. Phys. **4**, 130 (2008).
8. A. R. Maier, A. Meseck, S. Reiche, C. B. Schroeder, T. Seggebrock, and F. Grüner, Phys. Rev. X **2**, 031019 (2012).
9. F. Albert and A. G. Thomas, Plasma Phys. Control. Fusion **58**, 103001 (2016).
10. W. Wang, K. Feng, L. Ke, C. Yu, Y. Xu, R. Qi, Y. Chen, Z. Qin, Z. Zhang, M. Fang, J. Liu, K. Jiang, H. Wang, C. Wang, X. Yang, F. Wu, Y. Leng, J. Liu, R. Li, and Z. Xu, Nature **595**, 516 (2021).
11. G. Sarri, W. Schumaker, A. Di Piazza, M. Vargas, B. Dromey, M. E. Dieckmann, V. Chvykov, A. Maksimchuk, V. Yanovsky, Z. H. He, B. X. Hou, J. A. Nees, A. G. Thomas, C. H. Keitel, M. Zepf, and K. Krushelnick, Phys. Rev. Lett. **110**, 255002 (2013).
12. G. Sarri, D. J. Corvan, W. Schumaker, J. M. Cole, A. Di Piazza, H. Ahmed, C. Harvey, C. H. Keitel, K. Krushelnick, S. P. D. Mangles, Z. Najmudin, D. Symes, A. G. R. Thomas, M. Yeung, Z. Zhao, and M. Zepf, Phys. Rev. Lett. **113**, 224801 (2014).
13. B. Cros and P. Muggli, arXiv:1901.08436 (2019).
14. A. G. R. Thomas, C. P. Ridgers, S. S. Bulanov, B. J. Griffin, and S. P. D. Mangles, Phys. Rev. X **2**, 041004 (2012).
15. T. G. Blackburn, C. P. Ridgers, J. G. Kirk, and A. R. Bell, Phys. Rev. Lett. **112**, 015001 (2014).
16. J. M. Cole, K. T. Behm, E. Gerstmayr, T. G. Blackburn, J. C. Wood, C. D. Baird, M. J. Duff, C. Harvey, A. Ilderton, A. S. Joglekar, K. Krushelnick, S. Kuschel, M. Marklund, P. McKenna, C. D. Murphy, K. Poder, C. P. Ridgers, G. M. Samarin, G. Sarri, D. R. Symes, A. G. R. Thomas, J. Warwick, M. Zepf, Z. Najmudin, and S. P. D. Mangles, Phys. Rev. X **8**, 011020 (2018).

17. K. Poder, M. Tamburini, G. Sarri, A. Di Piazza, S. Kuschel, C. D. Baird, K. Behm, S. Bohlen, J. M. Cole, D. J. Corvan, M. Duff, E. Gerstmayr, C. H. Keitel, K. Krushelnick, S. P. D. Mangles, P. McKenna, C. D. Murphy, Z. Najmudin, C. P. Ridgers, G. M. Samarin, D. R. Symes, A. G. R. Thomas, J. Warwick, and M. Zepf, Phys. Rev. X **8**, 031004 (2018).
18. A. G. R. Thomas, Z. Najmudin, S. P. D. Mangles, C. D. Murphy, A. E. Dangor, C. Kamperidis, K. L. Lancaster, W. B. Mori, P. A. Norreys, W. Rozmus, and K. Krushelnick, Phys. Rev. Lett. **98**, 095004 (2007).
19. M. J. V. Streeter, S. Kneip, M. S. Bloom, R. A. Bendoyro, O. Chekhlov, A. E. Dangor, A. Döpp, C. J. Hooker, J. Holloway, J. Jiang, N. C. Lopes, H. Nakamura, P. A. Norreys, C. A. J. Palmer, P. P. Rajeev, J. Schreiber, D. R. Symes, M. Wing, S. P. D. Mangles, and Z. Najmudin, Phys. Rev. Lett. **120**, 254801 (2018).
20. C. Xia, J. Liu, W. Wang, H. Lu, W. Cheng, A. Deng, W. Li, H. Zhang, X. Liang, Y. Leng, X. Lu, C. Wang, J. Wang, K. Nakajima, R. Li, and Z. Xu, Phys. Plasmas **18**, 113101 (2011).
21. A. Sävert, S. P. D. Mangles, M. Schnell, E. Siminos, J. M. Cole, M. Leier, M. Reuter, M. B. Schwab, M. Möller, K. Poder, O. Jäckel, G. G. Paulus, C. Spielmann, S. Skupin, Z. Najmudin, and M. C. Kaluza, Phys. Rev. Lett. **115**, 055002 (2015).
22. J. Wang, J. Feng, C. Zhu, Y. Li, Y. He, D. Li, J. Tan, J. Ma, and L. Chen, Plasma Phys. Control. Fusion **60**, 034004 (2018).
23. C. J. Zhang, Y. Wan, B. Guo, J. F. Hua, C.-H. Pai, F. Li, J. Zhang, Y. Ma, Y. P. Wu, X. L. Xu, W. B. Mori, H.-H. Chu, J. Wang, W. Lu, and C. Joshi, Plasma Phys. Control. Fusion **60**, 044013 (2018).
24. J. Osterhoff, A. Popp, Z. Major, B. Marx, T. Rowlands-Rees, M. Fuchs, M. Geissler, R. Hörlein, B. Hidding, S. Becker, E. Peralta, U. Schramm, F. Grüner, D. Habs, F. Krausz, S. Hooker, and S. Karsch, Phys. Rev. Lett. **101**, 085002 (2008).
25. N. A. M. Hafz, T. M. Jeong, I. W. Choi, S. K. Lee, K. H. Pae, V. V. Kulagin, J. H. Sung, T. J. Yu, K.-H. Hong, T. Hosokai, J. R. Cary, D.-K. Ko, and J. Lee, Nat. Photonics **2**, 571 (2008).
26. A. R. Maier, N. M. Delbos, T. Eichner, L. Hübner, S. Jalas, L. Jeppe, S. W. Jolly, M. Kirchen, V. Leroux, P. Messner, M. Schnepp, M. Trunk, P. A. Walker, C. Werle, and P. Winkler, Phys. Rev. X **10**, 031039 (2020).
27. Z.-H. He, B. Hou, V. Lebailly, J. A. Nees, K. Krushelnick, and A. G. R. Thomas, Nat. Commun. **6**, 7156 (2015).
28. S. J. D. Dann, C. D. Baird, N. Bourgeois, O. Chekhlov, S. Eardley, C. D. Gregory, J.-N. Gruse, J. Hah, D. Hazra, S. J. Hawkes, C. J. Hooker, K. Krushelnick, S. P. D. Mangles, V. A. Marshall, C. D. Murphy, Z. Najmudin, J. A. Nees, J. Osterhoff, B. Parry, P. Pourmoussavi, S. V. Rahul, P. P. Rajeev, S. Rozario, J. D. E. Scott, R. A. Smith, E. Springate, Y. Tang, S. Tata, A. G. R. Thomas, C. Thornton, D. R. Symes, and M. J. V. Streeter, Phys. Rev. Accel. Beams **22**, 041303 (2019).
29. R. J. Shalloo, S. J. Dann, J. N. Gruse, C. I. Underwood, A. F. Antoine, C. Arran, M. Backhouse, C. D. Baird, M. D. Balcazar, N. Bourgeois, J. A. Cardarelli, P. Hatfield, J. Kang, K. Krushelnick, S. P. Mangles, C. D. Murphy, N. Lu, J. Osterhoff, K. Põder, P. P. Rajeev, C. P. Ridgers, S. Rozario, M. P. Selwood, A. J. Shahani, D. R. Symes, A. G. Thomas, C. Thornton, Z. Najmudin, and M. J. Streeter, Nat. Commun. **11**, 6355 (2020).
30. S. Jalas, M. Kirchen, P. Messner, P. Winkler, L. Hübner, J. Dirkwinkel, M. Schnepp, R. Lehe, and A. R. Maier, Phys. Rev. Lett. **126**, 104801 (2021).
31. M. Kirchen, S. Jalas, P. Messner, P. Winkler, T. Eichner, L. Hübner, T. Hülsenbusch, L. Jeppe, T. Parikh, M. Schnepp, and A. R. Maier, Phys. Rev. Lett. **126**, 174801 (2021).
32. G. M. Samarin, M. Zepf, and G. Sarri, J. Mod. Opt. **65**, 1362 (2018).
33. C. D. Baird, C. D. Murphy, T. G. Blackburn, A. Ilderton, S. P. Mangles, M. Marklund, and C. P. Ridgers, New J. Phys. **21**, 053030 (2019).
34. C. Arran, J. M. Cole, E. Gerstmayr, T. G. Blackburn, S. P. Mangles, and C. P. Ridgers, Plasma Phys. Control. Fusion **61**, 074009 (2019).
35. J. Lin, Q. Qian, J. Murphy, A. Hsu, A. Hero, Y. Ma, A. G. R. Thomas, and K. Krushelnick, Phys. Plasmas **28**, 083102 (2021).
36. W. Rawat and Z. Wang, Neural Comput. **29**, 2352 (2017).
37. A. Kristiadi, M. Hein, and P. Hennig, in *Proceedings of the 37th International Conference on Machine Learning* (2020), p. 5436.
38. C. Emma, A. Edelen, M. J. Hogan, B. O'Shea, G. White, and V. Yakimenko, Phys. Rev. Accel. Beams **21**, 112802 (2018).
39. X. Ren, A. Edelen, A. Lutman, G. Marcus, T. Maxwell, and D. Ratner, Phys. Rev. Accel. Beams **23**, 040701 (2020).
40. A. Hanuka, C. Emma, T. Maxwell, A. S. Fisher, B. Jacobson, M. J. Hogan, and Z. Huang, Sci. Rep. **11**, 2945 (2021).
41. T. P. Rowlands-Rees, C. Kamperidis, S. Kneip, A. J. Gonsalves, S. P. D. Mangles, J. G. Gallacher, E. Brunetti, T. Ibbotson, C. D. Murphy, P. S. Foster, M. J. V. Streeter, F. Budde, P. A. Norreys, D. A. Jaroszynski, K. Krushelnick, Z. Najmudin, and S. M. Hooker, Phys. Rev. Lett. **100**, 105005 (2008).
42. A. Pak, K. A. Marsh, S. F. Martins, W. Lu, W. B. Mori, and C. Joshi, Phys. Rev. Lett. **104**, 025003 (2010).
43. C. McGuffey, A. G. R. Thomas, W. Schumaker, T. Matsuoka, V. Chvykov, F. J. Dollar, G. Kalintchenko, V. Yanovsky, A. Maksimchuk, K. Krushelnick, V. Y. Bychenkov, I. V. Glazyrin, and A. V. Karpeev, Phys. Rev. Lett. **104**, 025004 (2010).
44. M. Chen, E. Esarey, C. B. Schroeder, C. G. R. Geddes, and W. P. Leemans, Phys. Plasmas **19**, 033101 (2012).
45. D. P. Kingma and M. Welling, arXiv:1312.6114 (2013).
46. C. P. Burgess, I. Higgins, A. Pal, L. Matthey, N. Watters, G. Desjardins, and A. Lerchner, arXiv:1804.03599 (2018).
47. B. Xu, N. Wang, T. Chen, and M. Li, arXiv:1505.00853 (2015).
48. D. P. Kingma and J. Ba, arXiv:1412.6980 (2014).
49. F. Barnsley, B. Matthews, T. Griffin, J. W. A. Salt, D. Ross, C. Cătălin, A. Dibbo, and S. Y. Crompton, in *11th New Opportunities for Better User Group Software (NOBUGS)* (2016), p. 23.
50. W. Lu, M. Tzoufras, C. Joshi, F. Tsung, W. Mori, J. Vieira, R. Fonseca, and L. Silva, Phys. Rev. Spec. Top. Accel. Beams **10**, 061301 (2007).
51. M. S. Bloom, M. J. V. Streeter, S. Kneip, R. A. Bendoyro, O. Cheklov, J. M. Cole, A. Döpp, C. J. Hooker, J. Holloway, J. Jiang, N. C. Lopes, H. Nakamura, P. A. Norreys, P. P. Rajeev, D. R. Symes, J. Schreiber, J. C. Wood, M. Wing, Z. Najmudin, and S. P. D. Mangles, Phys. Rev. Accel. Beams **23**, 061301 (2020).
52. A. G. Thomas, S. P. D. Mangles, Z. Najmudin, M. C. Kaluza, C. D. Murphy, and K. Krushelnick, Phys. Rev. Lett. **98**, 054802 (2007).
53. T. Matsuoka, C. McGuffey, P. G. Cummings, Y. Horovitz, F. Dollar, V. Chvykov, G. Kalintchenko, P. Rousseau, V. Yanovsky, S. S. Bulanov, A. G. R. Thomas, A. Maksimchuk, and K. Krushelnick, Phys. Rev. Lett. **105**, 034801 (2010).